International Journal of Heat and Fluid Flow 76 (2019) 57–71

Contents lists available at ScienceDirect

International Journal of Heat and Fluid Flow

journal homepage: www.elsevier.com/locate/ijhff

Numerical modelling of a melting-solidification cycle of a phase-change material with complete or partial melting

Aina Rakotondrandisa[a], Ionut Danaila[a], Luminita Danaila[*,b]

[a] Laboratoire de Mathématiques Raphaël Salem, CNRS UMR 6085, Université de Rouen Normandie, Avenue de l'Université, BP 12, Saint-Étienne-du-Rouvray F-76801, France

[b] CORIA, CNRS UMR 6614, Université de Rouen Normandie, Avenue de l'Université, BP 12, Saint-Étienne-du-Rouvray F-76801, France

ARTICLE INFO

Keywords:
Phase change
PCM
Melting
Solidification
Navier–Stokes
Boussinesq
FreeFem + +
Newton method
Finite element
Mesh adaptivity

ABSTRACT

A high accuracy numerical model is used to simulate an alternate melting and solidification cycle of a phase change material (PCM). We use a second order (in time and space) finite-element method with mesh adaptivity to solve a single-domain model based on the Navier-Stokes-Boussinesq equations. An enthalpy method is applied to the energy equation. A Carman-Kozeny type penalty term is introduced in the momentum equation to bring the velocity to zero inside the solid region. The mesh is dynamically adapted at each time step to accurately capture the interface between solid and liquid phases, the boundary-layer structure at the walls and the multicellular unsteady convection in the liquid. We consider the basic configuration of a differentially heated square cavity filled with an octadecane paraffin and use experimental and numerical results from the literature to validate our numerical system. The first study case considers the complete melting of the PCM (liquid fraction of 95%), followed by a complete solidification. For the second case, the solidification is triggered after a partial melting (liquid fraction of 50%). Both cases are analysed in detail by providing temporal evolution of the solid-liquid interface, liquid fraction, Nusselt number and accumulated heat input. Different regimes are identified during the melting-solidification process and explained using scaling correlation analysis. Practical consequences of these two operating modes are finally discussed.

1. Introduction

The fundamental operational mode of latent thermal energy storage (LTES) systems based on phase-change materials (PCM) is made of alternate melting and solidification cycles that are not necessarily periodic. Partial melting and/or solidification of the PCM are often observed in applications and, in particular, in applications for buildings (Zhu et al., 2009; Ascione et al., 2014). Using the total latent heat storage potential offered by the PCM in energy storage requires a complex design process. This could benefit from accurate numerical simulations of such incomplete charging/discharging cycles. A wide range of recent applications is concerned by such modelling issues, including thermal energy storage (*e. g.* for solar power generation) and passive temperature control (*e. g.* for modern portable electronics) devices. For a review of various applications of PCMs with different melting temperatures in thermal energy storage systems, see recent reviews by Agyenim et al. (2010) and Kalnæs and Jelle (2015).

Actual challenges in the mathematical and numerical description of a melting-solidification cycle include (i) the derivation of a realistic theoretical framework, using transport equations for different involved quantities (velocity, temperature, viscosity, density) and (ii) the design of robust, accurate and efficient numerical methods for solving these equations, for different initial and boundary conditions.

As far as point (i) is concerned, the solution of the Stefan problem has been provided by Rubinstein (1947). Later, other important physical phenomena have been accounted for: gravity effects, convection in the liquid phase, the presence of a mushy region containing both solid and liquid parcels at the interface between the two phases, etc. For a comprehensive review of these approaches, see Kowalewski and Gobin (2004) and Faghri and Zhang (2006). A historical review of the role played by convection in phase-change problems is provided by e.g. Yao and Prusa (1989). In particular, the natural convection in the liquid was proved to play an important role in the heat transfer between phases and in the propagation of the melting/solidification front (Morgan, 1981; Voller and Prakash, 1987; Jany and Bejan, 1988; Evans et al., 2006; Vidalain et al., 2009; Wang et al., 2010a). As a

* Corresponding author.
E-mail addresses: aina.rakotondrandisa@etu.univ-rouen.fr (A. Rakotondrandisa), ionut.danaila@univ-rouen.fr (I. Danaila), luminita.danaila@coria.fr, danaila@coria.fr (L. Danaila).

https://doi.org/10.1016/j.ijheatfluidflow.2018.11.004
Received 16 May 2018; Received in revised form 4 November 2018; Accepted 5 November 2018

Nomenclature

c	specific heat, J/(kg K)
C	dimensionless specific heat
C_{CK}	penalty constant
f_B	Boussinesq force
Fo	Fourier number
g	gravitational acceleration, m/s^2
H	cavity height, m
h	enthalpy, J/kg
h_{sl}	latent heat of fusion, J/kg
k	thermal conductivity, W/(m K)
K	dimensionless thermal conductivity
L_f	liquid fraction
Pr	Prandtl number
Re	Reynolds number
Ra	Rayleigh number
Ste	Stefan number
Nu	Nusselt number
p	pressure, N/m^2
Q_0	accumulated heat input
t, τ	dimensionless times
t_φ	physical time, s
T	temperature, K
$\tilde{\boldsymbol{u}}$	velocity, m/s
$\boldsymbol{u}$	dimensionless velocity
$\tilde{\boldsymbol{x}}$	coordinates, m
$\boldsymbol{x}$	dimensionless coordinates

Greek

α	thermal diffusivity, m^2/s
β	thermal expansion coefficient, 1/K
μ	dynamic viscosity, kg/(m s)
ν	kinematic viscosity, m^2/s
ρ	density, kg/m^3
θ	dimensionless temperature

Subscripts

ref	reference state
s, l	solid, liquid
h, c	hot, cold
f	fusion
co	cooling

Reference quantities

δT	$T_h - T_f$
δT_{co}	$T_f - T_{co}$
r_δ	$(\delta T_{co})/\delta T$

consequence, modern simulations of phase-change systems are dealing with the Navier–Stokes equations for the liquid phase, using the Boussinesq approximation for thermal effects.

Single domain approaches are very convenient for numerical implementations, since the same system of Navier–Stokes–Boussinesq equations is solved inside both liquid and solid phases. Two ingredients are necessary to make possible the use of the single domain model. First, the velocity inside the solid phase has to be set to zero. This is achieved by directly setting the velocity to zero in finite-volume methods (*e. g.*, Wang et al. (2010a,b)) or by using penalty models in finite-elements methods, based on viscosity (Danaila et al., 2014) or Carman-Kozeny terms (Belhamadia et al., 2012; Zhang et al., 2015; Mencinger, 2004). Second, the energy equation is written using an enthalpy-based model (Voller et al., 1987; Cao et al., 1989; Cao and Faghri, 1990). The feature of the enthalpy method is its capability to deal with both mushy and single point phase changes. Indeed, in case of non-isothermal phase change, a mushy zone between the liquid and the solid phases characterizes the system. In case of pure materials, the phase change occurs at a fixed temperature; however an artificial mushy-zone is introduced between the solid and the liquid parts, just to regularize the enthalpy and other discontinuous parameters.

The challenge for numerical systems solving the single-domain Navier–Stokes–Boussinesq model is to accurately capture the moving solid-liquid interface. The problem is even more challenging when several melting-solidification fronts, with distorted shapes are present (*e. g.* the solidification after a partial melting). When fixed uniform meshes are used, which is the case of a great majority of existing finite-volume codes, the grid density has to be considerably increased in the entire domain, making the simulation very expensive. When a trade-off between accuracy and computational cost is sought, the fixed grid approach allows to place only a few computational cells inside the regularization region.

Dynamical mesh adaptivity becomes in this context a valuable tool to concentrate the grid refinement effort only in regions displaying high gradients of the computed variables (melting-solidification fronts, thermal or viscous boundary layers). For the classical two-phase Stefan problem, Belhamadia et al. (2004a) suggested an anisotropic mesh adaptation algorithm based on solution-dependent metrics. The authors extended their algorithm for the three-dimensional simulation of the same problem (Belhamadia et al., 2004b) and showed that the use of locally adapted meshes with strong anisotropy proved to be very effective in reducing the number of computational nodes for such phase-change systems without convection. To simulate melting or solidification problems with convection, Danaila et al. (2014) recently suggested a dynamical mesh adaptation algorithm based on metrics control and implemented with the FreeFem++ software (Hecht et al., 2007; Hecht, 2012). The advantage of this adaptive finite-element method, which will be also used in the present study, is to make possible, with reasonable computational cost, the re-meshing of the computational domain at each time step. A very refined discretization of the regularization zone between solid and liquid phases is thus obtained, while regions with low gradients are de-refined in order to balance the overall computational effort.

The previously mentioned modern numerical approaches were mostly applied to simulate separately melting or solidification problems and only recently for alternate melting and solidification cycles (Wang et al., 2010b). However, cyclic or periodic, melting and solidification problems have attracted considerable attention in the literature. Ho and Chu (1993) and Voller et al. (1996) studied numerically periodic melting in a square enclosure. Recently, Hosseini et al. (2014) presented experimental studies for the melting and the solidification of a cylindrical PCM during a charging and discharging process and Chabot and Gosselin (2017) studied analytically the effect of an alternate heating and cooling in a cylindrical PCM, with periodic boundary conditions.

The present contribution is scoped to offer an accurate numerical description of the alternate melting and solidification of a typical PCM. We use a finite-element numerical system with second-order accuracy in time and space to solve the single-domain model based on Navier–Stokes equations with Boussinesq approximation. The main advantage of our method is that the mesh adaptivity algorithm could be applied each time step. The mesh is thus dynamically refined with respect to velocity and temperature variables, allowing to accurately capture the interface between solid and liquid phases, the boundary-

layer structure at the walls and the details of the unsteady convection cells in the liquid.

We simulate a typical PCM configuration represented by a differentially heated square cavity filled with an octadecane paraffin. This is a well-established benchmark documented experimentally by Okada (1984) and extensively used to validate numerical codes (Wang et al., 2010a; Jany and Bejan, 1988; Mencinger, 2004). First, we simulate the melting phase and use this case to validate our numerical system against experimental and previously reported numerical data. Second, we consider two operating cases for the solidification process. In the first study case the solidification starts after a complete melting of the PCM (liquid fraction of 95%), while in the second case after a partial melting (liquid fraction of 50%). All cases are analysed in detail by providing temporal evolution of solid-liquid interface, liquid fraction, Nusselt number and accumulated heat input. Different heat transfer regimes are identified and explained using scaling correlation theory. Several practical implications for the two operating modes are finally drawn.

The paper is organized as follows. Section 2 introduces the governing equations. Section 3 presents the numerical system. The final Section 4 is devoted to extensive analysis of the results for the two operating cases.

2. Governing equations

We consider a solid-liquid system placed in a two-dimensional square cavity of height H. In the following, subscripts s and l will refer to the solid and liquid phases, respectively.

For the numerical implementation, it is convenient to adopt a single-domain approach to describe both phases using the same system of equations. The model is based on the Navier–Stokes equations with Boussinesq approximation, which is the natural description of the fluid flow with natural convection. A penalty term is added to the momentum equations to bring the velocity to zero inside the solid region. For the energy conservation equation, an enthalpy method is used to model the phase change process. The single-domain model is described in detail in the following sections.

2.1. Enthalpy method

The phase change process is modelled using an enthalpy method (Voller et al., 1987; Cao et al., 1989; Cao and Faghri, 1990) with temperature-based formulation. We start from the energy equation:

$$\frac{\partial(\rho h)}{\partial t_\varphi} + \nabla\cdot(\rho h\tilde{\boldsymbol{u}}) - \nabla\cdot(k\nabla T) = 0, \tag{1}$$

where t_φ is the physical time, h the enthalpy, ρ the density, $\tilde{\boldsymbol{u}}$ the velocity vector, T the temperature and k the thermal conductivity. To make Eq. (1) valid for the entire domain containing both liquid and solid phases, the total enthalpy h is regarded as the sum of the sensible heat and the latent heat:

$$h = c(T + s(T)), \tag{2}$$

with c the local specific heat. The function $s(T)$ is introduced to model the jump of the enthalpy due to the phase change and is theoretically a Heaviside step function depending on the temperature: it takes the zero value in the solid region and a large value in the liquid, equal to h_{sl}/c, with h_{sl} the latent heat of fusion. Linear (Voller et al., 1987; Wang et al., 2010a) or smoother functions (Danaila et al., 2014) can be used to regularize $s(T)$ and also the jump of material properties (from solid to liquid). In this paper we use a regularization of all step-type functions by a continuous and differentiable hyperbolic-tangent function suggested by Danaila et al. (2014) (see below). We assume moreover that the undercooling phenomenon is negligible (see also Wang et al. (2010b); Kowalewski and Gobin (2004)).

Equation (1) can be further simplified by considering the following assumptions: (i) the density difference between solid and liquid phases is negligible, *i. e.* $\rho_l = \rho_s = \rho$ is constant; (ii) the regularization zone is narrow and the velocity inside this zone is very low. Consequently, the final expression of the energy equation is obtained by combining (2) and (1) and neglecting the convection term $\nabla\cdot(cs\tilde{\boldsymbol{u}})$[1]:

$$\frac{\partial(cT)}{\partial t_\varphi} + \nabla\cdot(cT\tilde{\boldsymbol{u}}) - \nabla\cdot\left(\frac{k}{\rho}\nabla T\right) + \frac{\partial(cs)}{\partial t_\varphi} = 0. \tag{3}$$

Furthermore, the essential feature of the current approach is that the phase change front is not tracked explicitly but is instead recovered a posteriori from the computed temperature field.

2.2. Navier-Stokes equations with Boussinesq approximation

The natural convection in the liquid part of the system is modelled using the incompressible Navier–Stokes equations, with Boussinesq approximation for buoyancy effects. To make this model valid for both liquid and solid phases, the momentum equation is modified as follows:

$$\frac{\partial\tilde{\boldsymbol{u}}}{\partial t_\varphi} + (\tilde{\boldsymbol{u}}\cdot\nabla)\tilde{\boldsymbol{u}} + \frac{1}{\rho}\nabla p - \frac{\mu_l}{\rho}\nabla^2\tilde{\boldsymbol{u}} - f_B(T)\boldsymbol{e}_y = A(T)\tilde{\boldsymbol{u}}, \tag{4}$$

where p denotes the pressure, μ_l the dynamic viscosity of the liquid (assumed to be constant) and $f_B(T)$ the Boussinesq force. The penalty term $A(T)\tilde{\boldsymbol{u}}$ is artificially introduced in (4) to extend this equation in the solid phase, where the velocity, pressure, viscosity and Boussinesq force are meaningless. Consequently, $A(T)$ is modelled to vanish in the liquid, where the Navier–Stokes–Boussinesq momentum equation is recovered. A large value of $A(T)$ is imposed in the solid, reducing the momentum Eq. (4) to $A(T)\tilde{\boldsymbol{u}} = 0$, equivalent to $\tilde{\boldsymbol{u}} = 0$. Exact expressions for f_B and A will be given in the next section.

Finally, the conservation of mass in the liquid phase is expressed by the continuity equation:

$$\nabla\cdot\tilde{\boldsymbol{u}} = 0. \tag{5}$$

2.3. Final system of equations for the single-domain approach

It is convenient to numerically solve a dimensionless form of the previous equations. Using the cavity height H as length scale and a reference state (ρ, V_{ref}, T_f), we can define the following scaling for the space, velocity, temperature and time variables:

$$\boldsymbol{x} = \frac{\tilde{\boldsymbol{x}}}{H},\ \boldsymbol{u} = \frac{\tilde{\boldsymbol{u}}}{V_{ref}},\ \theta = \frac{T - T_f}{\delta T},\ t = \frac{V_{ref}}{H}t_\varphi, \tag{6}$$

Temperatures T_h (hot) and T_c (cold) will be used to set isothermal walls of the cavity. The difference $\delta T = T_h - T_f$, with T_f the temperature of fusion, is considered as the representative temperature scale for the natural convection onset in the liquid region. As far as the solidification process is concerned, a distinct discussion will be provided in Section 4.3. Thus δT is used to define the Rayleigh number of the flow:

$$Ra = \frac{g\beta H^3\delta T}{\nu_l\alpha_l}, \tag{7}$$

where $\alpha = k/(\rho c)$ is the thermal diffusivity and β the thermal expansion coefficient. Note that the reference temperature in this scaling is T_f, resulting in $\theta_f = 0$. This simplifies the identification of the regularization zone, defined for $-\varepsilon \le \theta \le \varepsilon$.

Finally, the dimensionless system of equations to be solved in both liquid and solid regions can be written as:

$$\nabla\cdot\boldsymbol{u} = 0, \tag{8}$$

[1] In the liquid phase, $\nabla\cdot(cs\tilde{\boldsymbol{u}}) = h_{sl}\nabla\cdot\tilde{\boldsymbol{u}} = 0$; in the solid phase, $s = 0$; in the regularization region, it is assumed that $\tilde{\boldsymbol{u}} = 0$.

$$\frac{\partial \boldsymbol{u}}{\partial t} + (\boldsymbol{u}\cdot\nabla)\boldsymbol{u} + \nabla p - \frac{1}{Re}\nabla^2\boldsymbol{u} - f_B(\theta)\boldsymbol{e}_y - A(\theta)\boldsymbol{u} = 0, \tag{9}$$

$$\frac{\partial (C\theta)}{\partial t} + \nabla\cdot(C\theta\boldsymbol{u}) - \nabla\cdot\left(\frac{K}{Re\mathrm{Pr}}\nabla\theta\right) + \frac{\partial (CS)}{\partial t} = 0, \tag{10}$$

where the linearised (Boussinesq) buoyancy force (f_B), the Reynolds (Re) and Prandtl (Pr) numbers are defined as:

$$f_B(\theta) = \frac{Ra}{\mathrm{Pr}Re^2}\theta, \quad Re = \frac{\rho V_{ref} H}{\mu_l} = \frac{V_{ref} H}{\nu_l}, \quad \mathrm{Pr} = \frac{\nu_l}{\alpha_l}. \tag{11}$$

Non-dimensional conductivity and specific heat are functions of the temperature θ,

$$K(\theta) = \frac{k}{k_l}, \quad C(\theta) = \frac{c}{c_l}, \tag{12}$$

and have to take into account the variation of material properties between the solid and the liquid regions.

In the energy Equation (10), the non-dimensional function $S = s/\delta T$, introduced by the enthalpy model, is regularized across the regularization region using a hyperbolic-tangent function (Danaila et al., 2014):

$$S(\theta) = S_l + \frac{S_s - S_l}{2}\left\{1 + \tanh\left(\frac{\theta_r - \theta}{R_r}\right)\right\}, \tag{13}$$

where θ_r is the central value around which we regularize (typically $\theta_r = \theta_f = 0$) and R_r the smoothing radius (typically $R_r = \varepsilon$). Note that $S_s = 0$ and

$$S_l = \frac{h_{sl}/c_l}{\delta T} = \frac{1}{Ste}, \tag{14}$$

where *Ste* is the Stefan number. Regularizations similar to (13) are used to model the variation inside the regularization region of functions (12) defining material properties.

Finally, the penalty term in the momentum Eq. (9) takes the form (Belhamadia et al., 2012; Kheirabadi and Groulx, 2015):

$$A(\theta) = -\frac{C_{\mathrm{CK}}(1-\varphi(\theta))^2}{\varphi(\theta)^3 + b}, \tag{15}$$

where $\varphi(\theta)$ is the phase-change variable, which is 1 in the fluid region and 0 in the solid. Inside the regularization region, $\varphi(\theta)$ is regularized using a hyperbolic-tangent function similar to (13). The constant C_{CK} is set to a large value (as discussed below) and the constant $b = 10^{-6}$ is introduced to avoid division by zero.

3. Numerical method

To solve the system of Eqs. (8)–(10) we use a finite-element method that was implemented using the open-source software FreeFem++ (Hecht et al., 2007; Hecht, 2012), using a large variety of triangular finite elements to solve partial differential equations. FreeFem++ is an integrated product with its own high level programming language and a syntax close to mathematical formulations, making the implementation of numerical algorithms very easy. Among the numerous numerical tools offered by FreeFem++, the use of the powerful mesh adaptivity function proved mandatory in this study to obtain accurate results within reasonable computational time. The numerical code was optimized to afford the mesh refinement every time step: the mesh density was increased around the phase change interfaces, offering an optimal resolution of the large gradients of all regularized functions (*S, K, C, L_F*), while the mesh was de-refined (larger triangles) in the solid part, where a coarser mesh could be used. A simulation using a globally refined mesh would require a prohibitive computational time for an equivalent accuracy of the melting front resolution. Similar algorithms based on FreeFem++ were successfully used for solving different systems of equations with locally sharp variation of the solution, such as Gross–Pitaevskii equation (Danaila and Hecht, 2010; Vergez et al., 2016) or Laplace equations with nonlinear source terms (Zhang and Danaila, 2013).

The space discretization is based on Taylor–Hood finite elements, approximating the velocity with P_2 Lagrange finite elements (piecewise quadratic), and the pressure with the P_1 finite elements (piecewise linear). The temperature and the enthalpy are discretized using P_1 finite elements. The weak formulation of (8)–(10), necessary for the finite-element implementation is described in detail in Danaila et al. (2014). There are two novelties in the present numerical approach, when compared to Danaila et al. (2014): *(i)* we use an approach based on the Carman–Kozeny model to bring the velocity to zero inside the solid phase, as described in the previous section, instead of the viscosity penalty method (imposing a large value of the viscosity in the solid); *(ii)* we increase the time accuracy of the algorithm by replacing the first-order Euler scheme with the second-order Gear (BDF2) scheme (see also Belhamadia et al. (2012)),

$$\frac{d\phi}{dt} \simeq \frac{3\phi^{n+1} - 4\phi^n + \phi^{n-1}}{2\delta t}, \tag{16}$$

computing the solution ϕ^{n+1} at time $t_{n+1} = (n+1)\delta t$ by using two previous states (ϕ^n, ϕ^{n-1}). We use this scheme to advance in time both velocity ($\phi = \boldsymbol{u}$) and temperature fields ($\phi = \theta$). The other terms in Eqs. (8)–(10) are treated implicitly (*i. e.* taken at time t_{n+1}). The resulting non-linear equations are solved using a Newton algorithm.

3.1. Mesh adaptivity

Mesh adaptivity by metric control is a standard function offered by FreeFem++ (Hecht, 2012). The key idea for the mesh adaptivity (see also Castro-Diaz et al. (2000); Hecht and Mohammadi (1997); George and Borouchaki (1998)) is to modify the scalar product used in an automatic mesh generator to evaluate distance and volume, in order to construct equilateral elements according to a new adequate metric. The scalar product is based on the evaluation of the Hessian $\mathcal{H}$ of the variables of the problem. Indeed, for a P_1 discretization of a variable χ, the interpolation error is bounded by:

$$\mathcal{E} = |\chi - \Pi_h\chi|_0 \le c \sup_{T\in\mathcal{T}_h} \sup_{x,y,z\in T} |\mathcal{H}(x)|(y-z, y-z) \tag{17}$$

where $\Pi_h\chi$ is the P_1 interpolate of χ, $|\mathcal{H}(x)|$ is the Hessian of χ at point x after being made positive definite. We can infer that, if we generate, using a Delaunay procedure (e.g. George and Borouchaki (1998)), a mesh with edges close to the unit length in the metric $\mathcal{M} = \frac{|\mathcal{H}|}{(c\mathcal{E})}$, the interpolation error $\mathcal{E}$ will be equally distributed over the edges a_i of the mesh. More precisely, we have

$$\frac{1}{c\mathcal{E}} a_i^T \mathcal{M} a_i \le 1. \tag{18}$$

The previous approach could be generalized for a vector variable $\chi = [\chi_1, \chi_2]$. After computing the metrics $\mathcal{M}_1$ and $\mathcal{M}_2$ for each variable, we define a metric intersection $\mathcal{M} = \mathcal{M}_1 \cap \mathcal{M}_2$, such that the unit ball of $\mathcal{M}$ is included in the intersection of the two unit balls of metrics $\mathcal{M}_2$ and $\mathcal{M}_1$ (for details, see the procedure defined in Frey and George (1999)).

For the cases considered in this study, we used five metrics intersection to adapt the mesh, based on S^{n+1}, S^n, T^{n+1}, T^n, $\boldsymbol{u}^{n+1}$. To reduce the impact of the interpolation on the global accuracy for time-depending problems, we consider the metrics computed from actual (at t_{n+1}) and previous (at t_n) values, for the same variable used for adaptivity (see also Belhamadia et al. (2004a)). The anisotropy of the mesh is a parameter of the algorithm and it was set to values close to 1. This is an inevitable limitation since we also impose the minimum edge-length of triangles to avoid generating a too large number of nodes.

Some examples of the adapted mesh generated during the computation of the solidification phase are given in Section 4.3. The method is

able to accurately capture the liquid-solid interface during the melting process and the two solidification fronts appearing during the solidification of the PCM. Mesh adaptivity is performed at each time step and offers a refined discretization of the regularization region where sharp gradients have to be accurately captured. The number of triangles for the melting case is $N_t = 12,000$ and $N_t = 17,000$ for the solidification phase. Non-adapted grids offering the same spatial resolution everywhere inside the computational domain would have resulted for the two cases in $N_t = 9.94{\cdot}10^{10}$ and $N_t = 10{\cdot}10^{10}$ triangles, respectively. Consequently, mesh adaptivity greatly helps in reducing the computational time.

4. Results

The basic configuration considered in this study is that used in the experimental study of Okada (1984). It consists of a differentially heated square cavity (see Fig. 1a), filled with an octadecane paraffin. The physical (non-dimensional) parameters are: $Ra = 3.27{\cdot}10^5$, Pr = 56.2 and $Ste = 0.045$. We numerically investigate the following cases:

(i) First we proceed to the validation of our numerical method on the basis of the melting of the PCM. The material is initially solid ($\theta_0 = -0.01$) and melts progressively starting from the left boundary, maintained at the hot temperature $\theta_h = 1$. The right boundary is also isothermal with cold temperature $\theta_c = -0.01$. This case is a well established benchmark used to validate numerical codes for phase-change systems. Three simulations are carried out to demonstrate the accuracy and the robustness of our method. The first validation case reproduces the experimental study of Okada (1984), the second corresponds to the experimental investigation of Gong et al. (2015) and the last considers the numerical simulations presented in Bertrand et al. (1999). For the last cases, the melting front, the Nusselt number and the liquid fraction provided by our code are compared with experimental and numerical results.

(ii) The melting of the PCM (Fig. 1b). Having validated our code, we pay a closer attention to other physical characteristics of the melting, such as the temporal evolution of the temperature distribution in the cavity, the Nusselt number, etc. We discuss and compare our results with those previously published: experimental (Okada, 1984) and numerical (Okada, 1984; Wang et al., 2010a; Ma and Zhang, 2006; Danaila et al., 2014). The scaling formulae suggested by Jany and Bejan (1988) are used to validate the Nusselt number of our simulation. This is described in Section 4.2.

(iii) After the complete melting of the PCM (*i. e.* the melting front is very close to the right wall and the liquid fraction is 0.95), we trigger the solidification process by cooling the left-wall below the fusion temperature, at a temperature θ_{co}, whilst the right wall is still kept at $\theta_c = -0.01$. Note that, as discussed later, θ_{co} and θ_c are not necessarily equal. The solid phase will propagate into the cavity from both left and right sides (Fig. 1c). This case is computationally challenging, since two melting/solidification fronts have to be accurately followed during the simulation. The process is simulated up to the complete solidification of the PCM and the non-trivial evolution of the liquid phase is depicted in detail. This case is described in Section 4.3.1.

(iv) This case is similar to the previous one, but the solidification starts after a partial melting of the PCM (*i. e.* the melting front is located approximatively at half distance between the two vertical walls and the liquid fraction is 0.5). The analysis of this case attempts to provide answers about the effectiveness of different possible functioning cycles of the PCM. This case is described in Section 4.3.2.

4.1. Numerical validation

We validate our numerical method against experimental and numerical studies of the melting of the octadecane PCM available in the literature. Three cases are investigated. The first consists of an experimental study of the melting of the PCM in a differentially heated square cavity of height $H = 1.5$ cm by Okada (1984). The second reproduces the melting of the PCM included in a transparent building brick of height $H = 15.2$ cm, investigated experimentally and numerically by Gong et al. (2015). The last compares our results with various numerical methods, presented by Bertrand et al. (1999), simulating the melting of octadecane, considering a higher value of the Rayleigh number.

For the simulation of the melting process (Fig. 1b), we use the following choice for the scaling introduced in Section 2.3, Eqs. (6) and (11):

$$V_{ref} = \frac{\nu_l}{H} \Rightarrow t = t_\varphi \frac{\nu_l}{H^2} \Rightarrow Re = 1. \tag{19}$$

Moreover, a second dimensionless time τ is introduced in order to assess our results with respect to the numerical data of Bertrand et al. (1999) and the analytical correlation of Jany and Bejan (1988):

$$\tau = Ste{\cdot}Fo = Ste{\cdot}\frac{\alpha t_\varphi}{H^2} = Ste{\cdot}\frac{t}{Pr}, \tag{20}$$

where *Fo* is the Fourier number.

We first examine the location of the interface obtained in our simulations. The comparison with the experimental results of Okada (1984) and Gong et al. (2015) is presented in Fig. 2. The experimental study of Okada (1984) in Fig. 2(a) consists of a differentially heated square cavity of dimensions 1.5 cm × 1.5 cm, filled with an octadecane paraffin. The non-dimensional parameters are: $Ra = 3.27{\cdot}10^5$, Pr = 56.2 and $Ste = 0.045$ (Benchmark 1).

For two particular time instants ($\tau = 0.032$ and $\tau = 0.063$), we could compare our results to available experimental (Okada, 1984) and numerical (Okada, 1984; Wang et al., 2010a; Danaila et al., 2014) data. In the experimental set up of Okada (1984), the author has reported that the top of the PCM was not perfectly insulated and consequently the growth of the experimental upper melting front was delayed. In

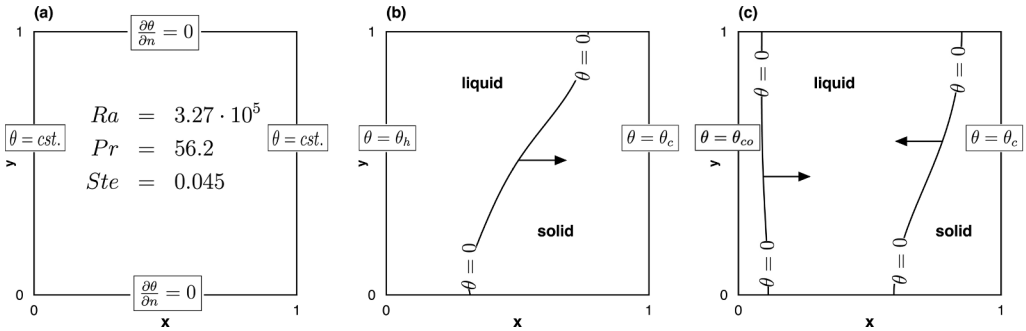

Fig. 1. Sketch of the computational domain and boundary conditions. General configuration (panel a) with isothermal ($\theta = cst.$) vertical ($x = 0$ and $x = 1$) walls and adiabatic ($\partial\theta/\partial n = 0$) top and bottom walls. Configuration for the melting phase (panel b) with a hot left wall ($\theta = \theta_h > 0$) and a cold right wall ($\theta = \theta_c < 0$), followed by a solidification phase (panel c), when the temperature of the left wall is cooled to $\theta = \theta_{co} < 0$.

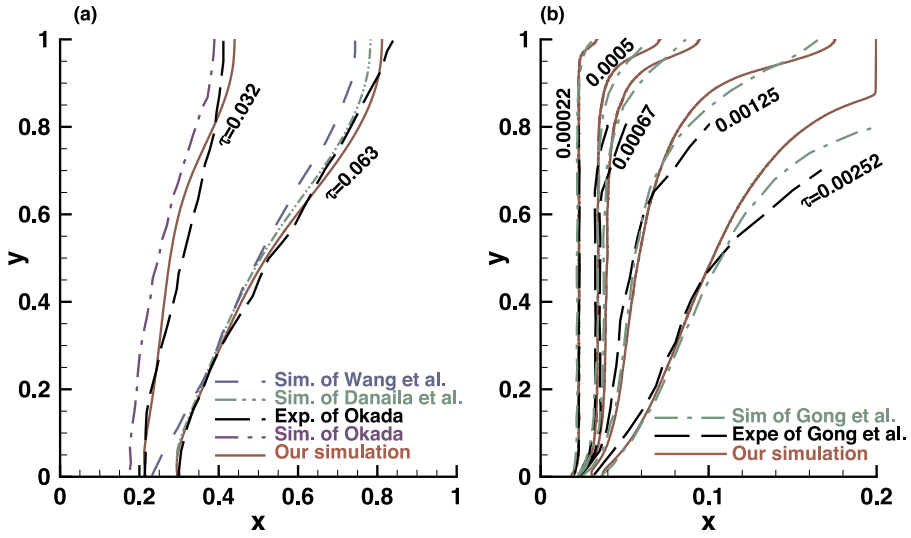

Fig. 2. Location of the interface during the melting of the PCM. (a) Comparison with experimental data of Okada (1984) and numerical results of Danaila et al. (2014) and Wang et al. (2010a) for two time instants ($\tau = 0.032$ and 0.063). Benchmark 1: $Ra = 3.27{\cdot}10^5$, Pr = 56.2 and $Ste = 0.045$ (b) Comparison with both experiment and simulation of Gong et al. (2015) for five time instants ($\tau = 0.0002$, 0.00050, 0.00067, 0.00125, 0.00252). Benchmark 2: $Ra = 2.48{\cdot}10^8$, Pr = 50 and $Ste = 0.072$.

Fig. 2(a), for the two time instants $\tau = 0.032$ and $\tau = 0.063$, the current work agrees well with the experimental results of (Okada, 1984) at the bottom part of the melting front. However, our results overestimate the location of the front in the top part of the cavity, which could be related to the experimental heat loss mentioned by the author.

Moreover, our results are qualitatively in a better agreement with experimental data than previously published numerical results. This is a direct consequence of the precise tracking of the melting front achieved by the mesh adaptivity performed at each time step. This assessment also allowed us to finely tune the value of the constants used in the model (15). Even though it is generally assumed that a large value for C_{CK} must be set, the exact value of this constant could influence the accuracy of the results (Kheirabadi and Groulx, 2015; Kumar and Krishna, 2017). This choice of the value of this constant is a still open problem. Very good agreement with the experimental result of Okada (1984) is obtained for C_{CK} varying in the range $[10^6, 10^8]$. Nevertheless, imposing a too large value $C_{CK} = 10^{10}$ results in artificially slowing the propagation of the melting front. We set for all subsequent simulations $C_{CK} = 10^6$.

Fig. 2(b) illustrates the interface location in the experiment and simulations of Gong et al. (2015), who studied the melting of an octadecane PCM inside a transparent building brick of dimensions 15.2 cm × 3 cm. Their numerical simulation has been performed using a Lattice Boltzmann method. The non-dimensional parameters were: $Ra = 2.48{\cdot}10^8$, Pr = 50 and $Ste = 0.072$ (Benchmark 2). The difficulty here compared to the first validation case is the presence of a stronger natural convection flow in the fluid due to the high value of the Rayleigh number. The location of the interface is compared for five particular time instants: $\tau = 0.0002$, 0.00050, 0.00067, 0.00125 and 0.00252. We notice a very good agreement with the numerical and the experimental data of Gong et al. (2015).

A last validation case is also investigated to test the robustness of the method. The physical parameters are: $Ra = 10^8$, Pr = 50 and $Ste = 0.1$ (Benchmark 3). Bertrand et al. (1999) compiled results provided by five different authors (Lacroix, Le Quéré, Gobin–Vieira, Delannoy and Binet–Lacroix). Results provided by these authors will be hereafter referred to as (say) 'Lacroix, from Bertrand et al. (1999)'. They have attempted a first comparison by taking several numerical methods to compute the basic configuration presented in this section. Two investigators among the five failed to predict the process and showed unrealistic behaviors (see Figs. 3 and 4): Lacroix and Delannoy seem to be insufficiently converged (Fig. 3), and Binet-Lacroix overestimates the average Nusselt number by more than 30% (Fig. 4). Hence, this collection of results allows us to compare our numerical method and check whether or not realistic results are obtained for complex physical configurations.

We further inspect the melting front, the temporal evolution of the liquid fraction L_f and the Nusselt number Nu at the left wall ($x = 0$), for each of the five methods presented by Bertrand et al. (1999). For the liquid fraction, the initial solid state corresponds to $L_f = 0$, while $L_f = 1$ indicates the complete melting of the PCM. The average Nusselt number Nu at $x = 0$ left boundary is defined as follows:

$$Nu = \int_0^1 \left(\frac{\partial \theta}{\partial x}\right)_{x=0} dy. \tag{21}$$

The phase-change interface for four time steps, $\tau = 5{\cdot}10^{-4}$, $\tau = 2{\cdot}10^{-3}$, $\tau = 6{\cdot}10^{-3}$ and $\tau = 1{\cdot}10^{-2}$ is represented in Fig. 3. Our results are for each case in fairly good agreement with those of Gobin and those of Le Quéré. Gobin uses a front-tracking method using a coordinate transformation with a finite volume method with a 62 × 42 grids. Le Quéré solved a single domain model using a second order scheme with a finite volume method with a 192 × 192 grids (Gobin and Le Quéré (2000)).

The time evolution of the Nusselt number and the liquid fraction are presented in Fig. 4. A very good agreement is obtained with Gobin and Le Quéré. A relative difference, less than 2% is noticed for the Nusselt number, and a dispersion, smaller than 4%, for the liquid fraction.

The high value of the Rayleigh number $Ra = 10^8$ results in a very demanding numerical test. The high velocity, inducing a very narrow thermal boundary layer can lead to unrealistic results and some numerical methods have failed. The interest of the mesh adaptation is clearly evidenced since we initially use only 40 × 40 grid points.

4.2. Melting of the PCM

After the validation of the code, we now pay a closer attention to the time evolution of different physical parameter of the system, during the melting phase. We recall that the reference temperature is the fusion temperature and thus $\theta_f = 0$. The regularization range is defined for $-\varepsilon_1 \leq \theta \leq \varepsilon_2$, with $\varepsilon_1 = \varepsilon_2 = 0.01$. For this case, the physical properties of the material are identical in both liquid and solid phases, and, consequently, we obtain from (12) that and $K(\theta) = 1$. This choice of the scaling was made to have the same set of parameters as in previous

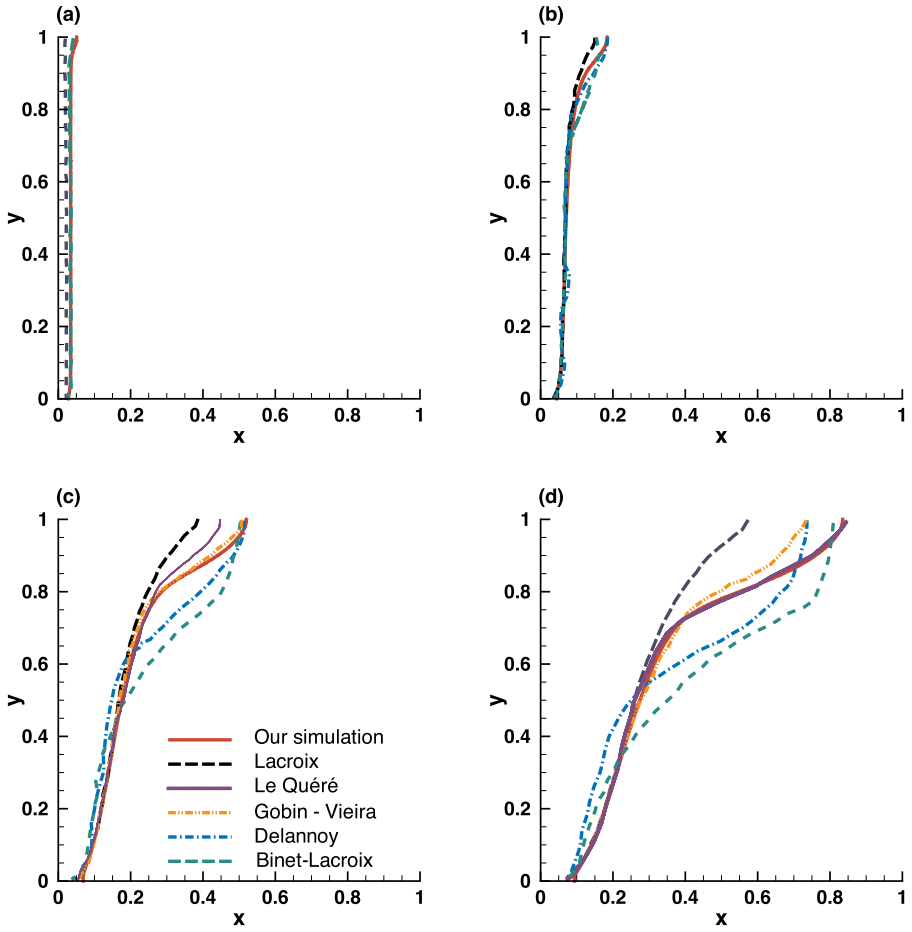

Fig. 3. Melting of a PCM (Benchmark 3). Location of the solid-liquid interface at dimensionless time (panels a to d) $\tau = 0.0005$, $\tau = 0.002$, $\tau = 0.006$ and $\tau = 0.01$, compared with five simulations presented by Bertrand et al. (1999). $Ra = 2{\cdot}10^8$, Pr = 50 and $Ste = 0.1$.

numerical simulations of this case (Okada, 1984; Wang et al., 2010a; Ma and Zhang, 2006; Danaila et al., 2014). The physical parameters correspond to the basic configuration presented in Fig. 1: $Ra = 3.27{\cdot}10^5$, Pr = 56.2 and $Ste = 0.045$.

4.2.1. Time evolution

We start by analysing the time evolution of the melting process. At $\tau = 0$, the material is solid and the initial temperature is set to $\theta = \theta_0 = -0.01$ everywhere inside the cavity. Then, the temperature of the left wall is suddenly increased to $\theta_h = 1$, while the right wall is maintained at the same cold temperature $\theta_c = -0.01$. The material starts to melt, with a melting front (identified by the isoline $\theta = \theta_f = 0$) propagating from the left to the right side of the domain. The time evolution of the phase-change system is depicted in Fig. 5 for representative time instants, also reported in previous studies.

From Fig. 5, we can easily identify three different regimes describing the time evolution of the melting process.

- From $\tau = 0$ to $\tau = 0.004$ (Fig. 5a), we note the vertical shape of the melting front, well predicted by the classical conduction model of

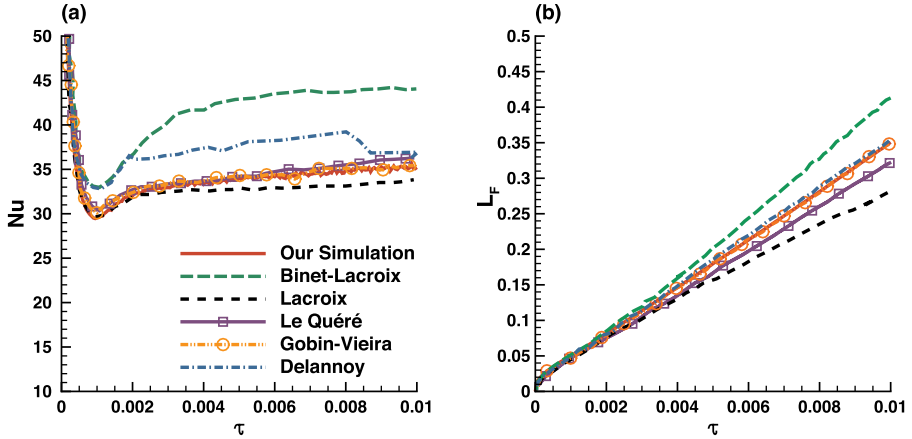

Fig. 4. Time evolution of the Nusselt number (a) and the liquid fraction (b) compared with five simulations presented by Bertrand et al. (1999). $Ra = 2{\cdot}10^8$, Pr = 50 and $Ste = 0.1$.

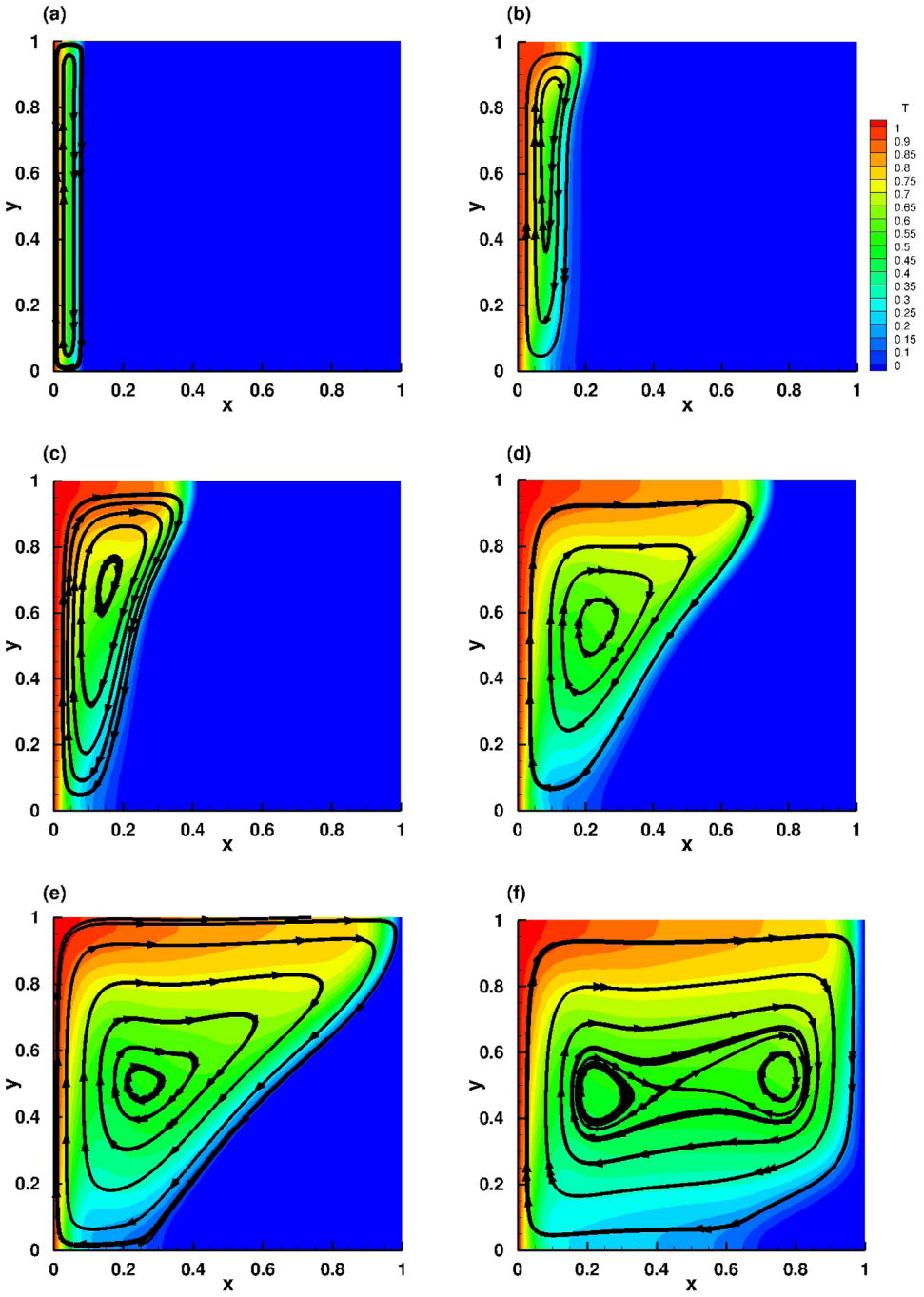

Fig. 5. Complete melting of the PCM. Temperature isolines and streamlines in the liquid phase. The solid part is represented in blue and corresponds to the region of temperature $\theta \leq \theta_f = 0$. Time instants (panels a to f): $\tau = 0.004$; 0.016; 0.032; 0.063; 0.08; 0.2. $Ra = 3.27{\cdot}10^5$, Pr = 56.2 and $Ste = 0.045$. (For interpretation of the references to colour in this figure legend, the reader is referred to the web version of this article.)

Stefan (1891). This indicates that, at this stage, heat transfer is dominated solely by conduction.

- Between $\tau = 0.016$ to $\tau = 0.032$ (Fig. 5b), the natural convection in the liquid phase starts to alter the shape of the melting front. A mixed conduction and convection regime rules the heat transfer. Convection mainly affects the upper part of the fluid motion, while conduction still dominates in the lower part. As the volumetric thermal expansion coefficient β is positive, we expect a clockwise circulation of the liquid inside the convection cell, as noted by Jany and Bejan (1988). This also makes the liquid-solid interface to move faster at the top of the cavity, explaining the deformed shape of the melting front, which is a signature of the convection effects (see also Kowalewski and Gobin (2004)).
- After $\tau = 0.032$ (Figs. 5c and d), natural convection dominates the heat transfer process and impacts radically the shape and motion of the solid-liquid interface. The melting front line exhibits four distinct regions characterized by different slopes with respect to the vertical axis. The largest slope is observed at the top of the cavity and is related to the particular shape of the convection cell. Note that top and bottom parts of the interface are normal to the cavity boundaries because of the imposed adiabatic boundary conditions.
- After $\tau = 0.08$ the melting front is nearly touching the right wall of the cavity, firstly at the top (Fig. 5e) of the cavity. The melting process continues and the fluid progressively fills the cavity, with a

melting front deforming into a vertical line. The simulation of the melting process is stopped at $\tau = 0.2$ (Fig. 5f), when it is numerically difficult to separate the melting front from the right wall boundary. At this time instant, the fluid fraction reaches the value of 0.95 and the melting of the PCM is considered to be complete, even though a small region of solid PCM remains at the lower right bottom of the cavity. Note from Fig. 5f the existence in the fluid of two recirculating zones instead of a single one observed during previous stages.

4.2.2. Scaling analysis

The melting of the octadecane was theoretically studied by Jany and Bejan (1988). Combining scaling theory and numerical modelling, they suggested closed-form correlations for the temporal evolution of the average Nusselt number (Nu) defined at the hot boundary ($x = 0$), under the form:

$$Nu(\tau) = \frac{1}{\sqrt{2\tau}} + \left[c_1 Ra^{1/4} - \frac{1}{\sqrt{2\tau}}\right]\left[1 + (c_2 Ra^{3/4}\tau^{3/2})^n\right]^{1/n}. \quad (22)$$

The values of the constants were fitted from numerical data: $c_1 = 0.27$, $c_2 = 0.0275$, and $n = -2$.

In Fig. 6 we compare the time evolution of the Nusselt number obtained from our numerical data (see Fig. 1) to experimental results of Okada (1984) and predictions obtained from the correlation (22). Our results perfectly fit the theoretical prediction of Jany and Bejan (1988). They are also in good agreement with experimental data, suggesting, however, that very accurate measurements and numerical simulations are needed to validate theoretical scaling analysis.

The time evolution of the Nusselt number can be correlated with the different heat transfer regimes analysed in the previous section:

1. A pure conduction regime for $\tau \gtrsim 0$ (corresponding to Fig. 5a), characterized by the law $Nu \sim (2\tau)^{-1/2}$. Since the temperature gradient has initially huge values because of the sudden increase of the temperature of the left wall, the Nusselt number rapidly decreases during the first stage of the flow evolution. The evolution law $Nu \sim \tau^{-1/2}$ can be also obtained from the Neumann exact solution supported by Grigull and Sandner (1984). The signature of this conduction regime is the slow heat transfer characterized by a monotonic decrease of the Nusselt number, down to a minimum corresponding to $\tau \sim Ra^{-1/2} = 0.02$.
2. A mixed conduction-convection regime for $0.02 \leq \tau \leq 0.05$ (illustrated in Fig. 5b). The influence of the Rayleigh number in (22) starts to be important and a good approximation for this regime is: $Nu \sim \tau^{-1/2} + Ra\,\tau^{3/2}$.
3. A convection dominated regime for $\tau > Ra^{-1/2}$ (corresponding to Figs. 5c–e). In the asymptotic limit of large τ, the simplified law $Nu \sim Ra^{1/4}$ is obtained. The plateau at the value of $Ra^{1/4}$ corresponds to the pure convective transfer and is observed in Fig. 6 for $0.05 \leq \tau \leq 0.1$. Numerical results show a slight decrease of the Nu in the final stage ($\tau \geq 0.1$), when the melting front starts to touch the right wall of the cavity (see Figs. 5e and f). The correlation model of Jany and Bejan (1988) is not valid for this late evolution of the melting process.

Another important basic quantity describing the melting process is the liquid fraction L_f. The time evolution of the liquid fraction (Fig. 7a) displays three regimes during the melting process. L_f initially grows as $\tau^{1/2}$, which is a typical law for a conduction-dominated heat transfer. Then, a linear evolution is observed, until the melting front reaches the right wall. This linear regime corresponds to the quasi-steady state observed in the evolution of the Nusselt number (Fig. 6).

Using the asymptotic limits of Eq. (22) for $\tau \to 0$ (pure conduction) and $\tau \to \infty$ (pure convection), Jany and Bejan (1988) suggested the following correlation law for the time evolution of the liquid fraction:

$$L_f(\tau) = \left[(\sqrt{2\tau})^5 + (c_1 Ra^{1/4}\tau)^5\right]^{1/5}, \quad (23)$$

where $c_1 = 0.27$ is the same constant as in (22). We compare in Fig. 7b our numerical results with the predictions based on (23) within the validity domain of the analysis, *i. e.* before the melting front reaches the right wall of the cavity. A very good agreement is found with theoretical predictions and also with previously published numerical results (Wang et al., 2010a).

4.2.3. Influence of the Rayleigh number

To assess on the influence of the Rayleigh number on the evolution of the melting process, we performed two other simulations by multiplying the initial value of $Ra = 3.27{\cdot}10^5$ by a factor of 5 and 10, respectively. The exact values are: $Ra = 1.62{\cdot}10^6$ and $Ra = 3.27{\cdot}10^6$. First, we increase the height H of the cavity by a factor of $\sqrt[3]{5}$ and $\sqrt[3]{10}$ and consider the same δT. Thus the Stefan number Ste is kept constant. Second, we increase the temperature difference parameter δT by keeping H constant. It corresponds of an increased value of the Stefan number by a factor of 5 and 10: $Ste = 0.223$ and $Ste = 0.45$. Figs. 8 and 9 show the temporal evolution of the liquid fraction L_f, and the average Nusselt number defined at the hot wall. The same heat transfer regimes described previously are observed for each case: conduction, mixed conduction-convection and convection.

Fig. 8(a) indicates that increasing the Rayleigh number by keeping δT constant induces a slower melting rate. This is the expected behaviour since the size of the PCM is increased by a factor of 2, and the velocity $\boldsymbol{u}$ is hence decreased to satisfy the condition $Re = 1$. We note however a non-monotonic variation of the time necessary to melt a fixed value of fluid. For instance, to achieve $L_f = 0.5$ (50% of the volume is melted), an increase of Ra by a factor of 10 leads to a growth of the melting time by a factor of 1.7. Nonetheless, when Ra is 5 times larger, the necessary time only increases by a factor of 2. This is most likely due to the non-linearity of the problem and requires further investigation. Furthermore, the Nusselt number reported in Fig. 8(b) shows that the higher the Rayleigh number is, the higher is the Nusselt number. This observation is consistent, since the temperature gradient is integrated along a greater heated wall.

Fig. 9(a) shows that by increasing the value of δT (and consequently increasing the Rayleigh number and the Stefan number), the PCM melts faster. We note that the height H of the cavity is kept constant, hence the natural convection flow in the melted PCM is enhanced when the Rayleigh number is increased. As a consequence, the convection-dominated regime is reached earlier, as shown by the shift of the minimum of the Nu to lower values of t_φ (Fig. 9(b)). This evolution is also observed for the liquid fraction. As expected, an increase of the

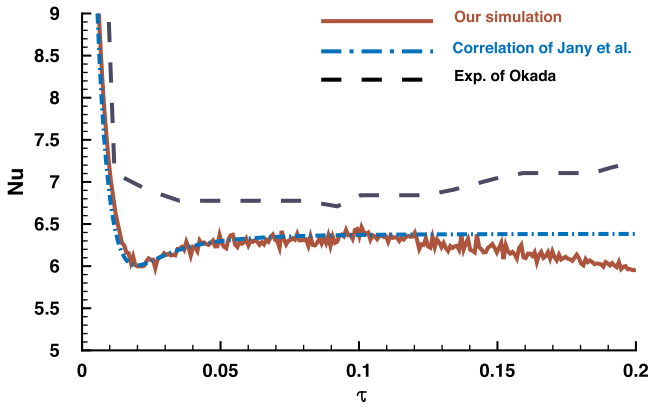

Fig. 6. Complete melting of the PCM. Time evolution of the average Nusselt number defined at the hot (left) wall (cf. Eq. (21)) (solid line). Comparison with the experimental results of Okada (1984) (dashed line) and the predictions using the correlation (22) suggested by Jany and Bejan (1988) (dash-dot line). $Ra = 3.27{\cdot}10^5$, Pr = 56.2 and $Ste = 0.045$ (Benchmark 1).

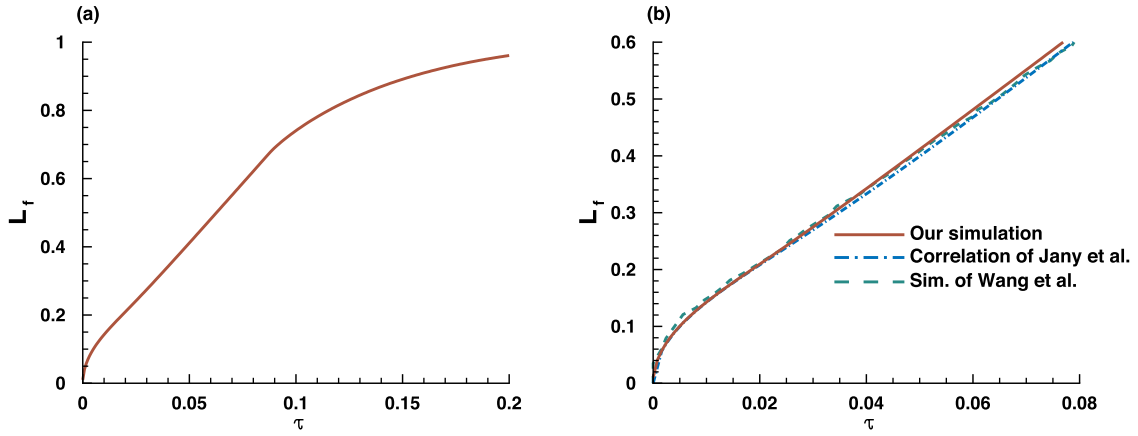

Fig. 7. Complete melting of the PCM (Benchmark 1). (a) Time evolution of the liquid fraction for the complete melting of the PCM. (b) Comparison of our results (solid line) with the numerical results of Wang et al. (2010a) (dashed line) and the predictions using the correlation (23) suggested by Jany and Bejan (1988) (dash-dot line).

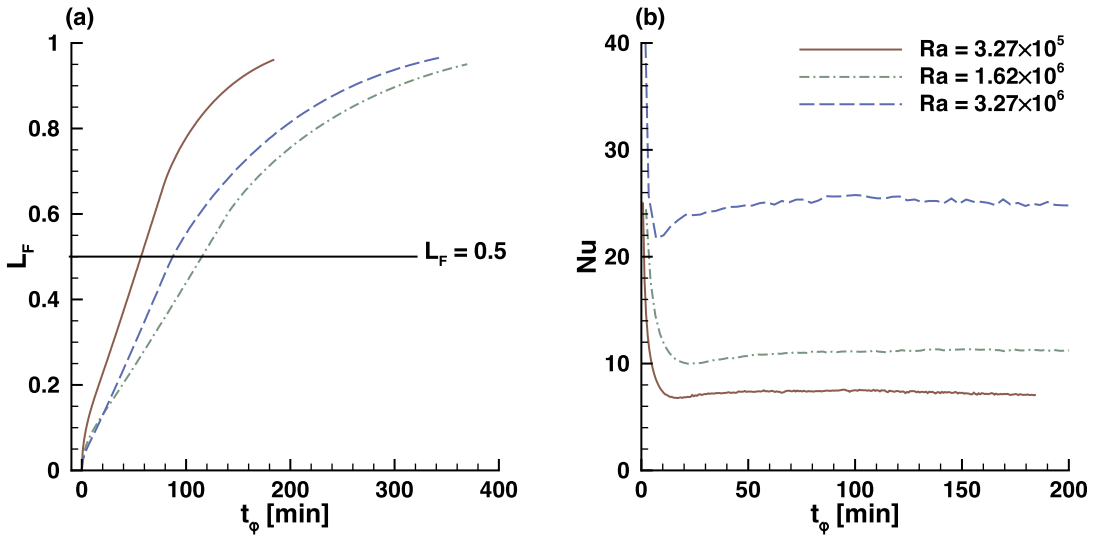

Fig. 8. Complete melting of the PCM. Influence of the value of the Rayleigh number (Ra) on the time evolution of the average Nusselt number defined at the hot (left) wall (a) and liquid fraction (b). The reference case ($Ra = 3.27{\cdot}10^5$) is represented by red continuous lines. The value of the Ra was increased by a factor of 5 and 10, respectively while the Stefan number (Ste) is kept constant. (For interpretation of the references to colour in this figure legend, the reader is referred to the web version of this article.)

Rayleigh and Stefan numbers is followed by an enhancement of the heat transfer during the melting, and consequently an improved efficiency of the PCM.

4.3. Solidification of the PCM

After the melting of the PCM, we simulate the solidification process. We consider two cases:

– case CM: solidification after a Complete Melting of the material ($L_f = 0.95$, Fig. 5f) and

– case PM: solidification after a Partial Melting ($L_f = 0.5$, Fig. 5d).

As emphasized previously, the natural convection occurring in the melting PCM is driven by the temperature difference $\delta T = T_h - T_f$. The dimensionless number that depicts the ratio between the forces creating and those refraining motion, is the Rayleigh number, which appears in the dimensionless form of the Navier–Stokes equations with Boussinesq approximation (Section 2). The higher is its value, the more intense is the heat transfer. Conversely, during the solidification, the phase-change is handled by the discharged temperature T_{co}, where the subscript 'co' stands for 'cooling'. In the geometry discussed in this paper, this represents the temperature of the left wall. Thus, the relevant temperature difference in the solid phase of the PCM is $\delta T_{co} = T_f - T_{co}$ and the dimensionless temperature in the solid phase should be defined with respect to this δT_{co}. It is then obvious, for Eqs. (7) and (11), that the Rayleigh number should be defined using the same temperature difference. However, because the Rayleigh number, as emphasized earlier, amounts for the motion created by hot temperature difference, we choose to keep the same definition for the Rayleigh number as for the melting case, still relevant for the melted core of the flow, where the persisting motion acts as a boundary condition for the solidification process. Under these conditions, in regard with the solidification process, we introduce a new parameter, $r_\delta = \delta T_{co}/(T_h - T_f)$, the normalised temperature is with respect to $T_f - T_{co}$ and the relevant Rayleigh number will then be $Ra_{co} = r_\delta \times Ra$, where Ra_{co} is the pseudo-Rayleigh number for solidification with a melted boundary. In the following, we will describe the process of solidification using three different values of r_δ. A new scaling is moreover introduced:

$$V_{ref} = \frac{\alpha_l}{H} \Rightarrow t = t_\varphi \frac{\nu_l}{H^2\,\mathrm{Pr}} \Rightarrow Re = \frac{1}{\mathrm{Pr}}. \tag{24}$$

The solidification stage is indeed a slower process compared to the melting, therefore the use of an adapted scaling is more relevant. This

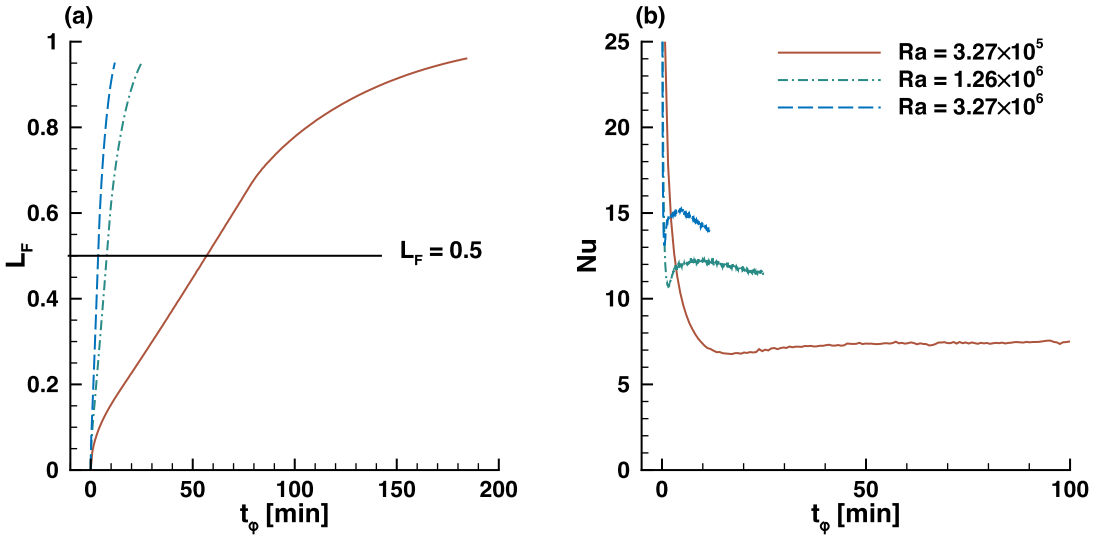

Fig. 9. Complete melting of the PCM. Influence of the value of the Rayleigh number (*Ra*) on the time evolution of the average Nusselt number defined at the hot (left) wall (a) and liquid fraction (b). The reference case ($Ra = 3.27{\cdot}10^5$) is represented by red continuous lines. The value of the *Ra* and *Ste* were increased by a factor of 5 and 10, respectively. (For interpretation of the references to colour in this figure legend, the reader is referred to the web version of this article.)

leads to a different time scaling for each cycle.

The simulation of the solidification process starts by imposing at the left-wall a constant (cooling) temperature.

The solid phase will propagate into the cavity from both left and right sides, which makes this case computationally challenging. The mesh adaptivity capabilities of our numerical code made possible to accurately track the two solidification fronts identified by the isoline $\theta = 0$. In the discussion below, the solidification process starts at physical time $t_\varphi = 185$ min (corresponding to $\tau = 0.2$) for case CM and at $t_\varphi = 59$ min ($\tau = 0.06$) for case PM.

4.3.1. Solidification after a complete melting. case CM.

The simulation continues from the state corresponding to Fig. 5 at $t_\varphi = 185$ min ($\tau = 0.063$) and solidification follows after a complete melting. Fig. 10 shows the evolution of the PCM during the solidification process. At $t_\varphi = 185$ min (Fig. 10a), the liquid fraction is $L_f = 0.95$ and the melting/solidification front is close to the right wall of the cavity. Setting a low temperature $\theta_{co} = -1$ at the left wall, while the right wall is maintained at a constant temperature ($\theta_{right} = -0.01 \leq \theta_f$) triggers the formation of a second solidification front, propagating from the left side of the domain. Figs. 10b and 10c illustrate the left part of the cavity solidifying at a faster rate because of the very low temperature imposed at the left wall, inducing a non symmetric evolution of the solid-liquid interfaces. The solid part is represented in blue and corresponds to the region of temperature $\theta \leq 0$. The signature of the conductive heat transfer is characterized by the vertical shape of the left front. Inside the liquid, the initial convection cells facilitate the heat transfer from the boundaries, resulting in a very rapid decrease of the fluid temperature. Temperature gradients being smoothed out during this first stage, the influence of the convection inside the liquid region is considerably reduced. As a result, the velocity inside the liquid is reduced to very low values. From $t_\varphi = 430$ min (Fig. 10d), the shape of both interfaces is almost symmetrical. This is a signature of a conduction dominated process. At $t_\varphi = 510$ min (Fig. 10e) the liquid region starts to shrink at the bottom side of the cavity. This process is accelerated and finally the liquid is trapped in a thin pocket and disappears completely through the top of the cavity (Fig. 10e). The complete solidification ends at $t_\varphi = 530$ min, *i. e.* the liquid fraction is $L_f = 0$. The adapted mesh, refined along the two solidification fronts, at $t_\varphi = 300$ min is reported in Fig. 10f, illustrating the efficiency of the adaptive mesh tool.

4.3.2. Solidification after a partial melting. case PM.

In this case, the solidification starts from the state corresponding to Fig. 11a at $t_\varphi = 59$ min ($\tau = 0.032$), when the liquid fraction is $L_f = 0.5$. The temperature of the left wall is suddenly lower at $\theta_{co} = -1$ as in the previous solidification simulation. The time evolution of the process is illustrated in Figs. 11a–e, while the adapted mesh corresponding to $t_\varphi = 90$ min is plotted in Fig. 11f. As in the previous case, a second solidification front starts to propagate from the left side of the cavity. The straight shape of the left solid front is always observed while the right solid front is impacted by the convection cell present in the central liquid region (Fig. 11b). The stronger convective effect is most likely due to the huge temperature difference that occurs over a smaller space distance (almost half of the volume is occupied by the solid state). This leads to stronger temperature gradients in the liquid region, and consequently to a stronger heat transfer. The two fronts merge to form a pocket of fluid which is connected to the top of the cavity (Figs. 11c–e). It is interesting to note that, as in the previous solidification case, the left part is solidifying at a faster rate, hence the pocket of melted PCM disappears completely from the right at the top side of the cavity (Figs. 11c–e).

4.4. Analysis of the solidification cycle from two different initial conditions: complete and partial melting. cases CM and PM.

The aim of this subsection is to investigate the temporal evolution of some physical properties of the solidification process, from two different initial conditions: (i) completely melted volume (case CM) and ii) partially melted volume (50% of the fluid is melted, case PM).

Fig. 12 represents the temporal evolution of the liquid fraction, the average Nusselt number (calculated at the cooled wall defined similarly to (21) and the accumulated heat input Q_0, for the two investigated cases. Q_0 is defined as follows:

$$Q_0 = \int_0^{t_\varphi} Nu \, dt_\varphi, \tag{25}$$

Simulations for three values $r_\delta = 1$, $r_\delta = 5$ and $r_\delta = 10$ are carried out.

Fig. 12(a) illustrates the temporal evolution of the liquid fraction L_f for the CM case. Complete melting occurs for $t_\varphi = 185$ min, after which solidification starts, with a continuous decrease of L_f till complete solidification is achieved. For the lowest value of r_δ, corresponding to $Ra_{co} = 3.27{\cdot}10^5$, the solidification process ends at $t_\varphi = 530$ min. Then, the higher value of r_δ is, the faster the discharge process is, with final

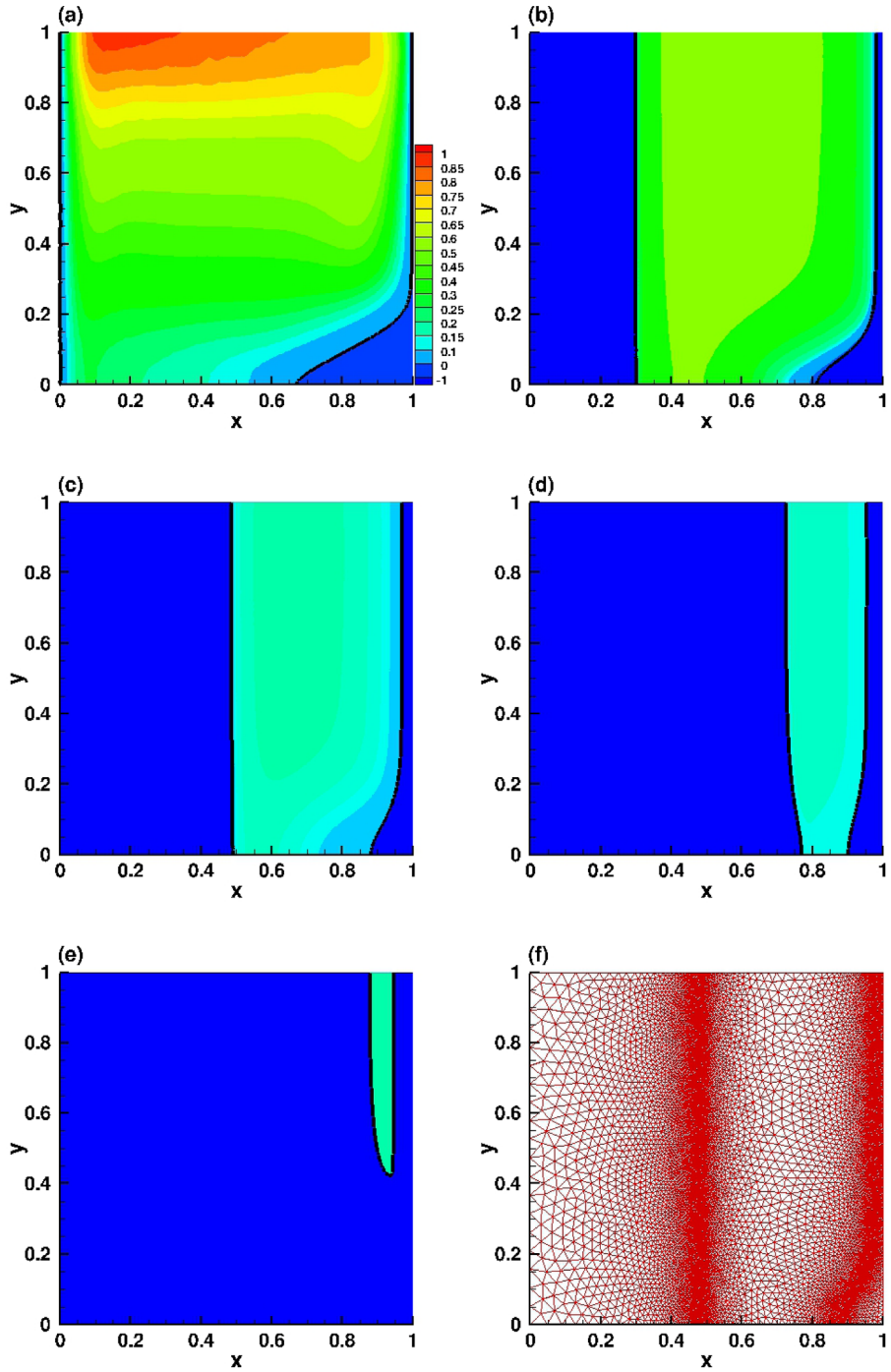

Fig. 10. Solidification of the PCM after a complete melting. Temperature isolines in the liquid phase. The solid part is represented in blue and corresponds to the region of temperature $\theta_{co} \leq \theta_f = 0$. Time instants (panels a to e): $t_\varphi = 185$ min, $t_\varphi = 231$ min, $t_\varphi = 300$ min, $t_\varphi = 430$ min and $t_\varphi = 510$ min. The adapted mesh corresponding to $t_\varphi = 300$ min is plotted in panel (f). $Ra_{co} = 3.27{\cdot}10^5$. (For interpretation of the references to colour in this figure legend, the reader is referred to the web version of this article.)

times $t_\varphi = 260$ min and $t_\varphi = 230$ min for cases $Ra_{co} = 1.62{\cdot}10^6$ and $Ra_{co} = 3.27{\cdot}10^6$, i.e. a drop of the cold boundary temperature by a factor of 5 and 10 respectively. The solidification speed, quantified by dL_f/dt_φ is nearly constant during almost the whole process for each case. This uniformity of the process indicates that the natural convection flow vanishes during the solidification, and conduction remains the only heat transfer mode.

Fig. 12(b) plots the temporal evolution of L_f for the PM case. As previously discussed, 50% of the volume is melted, at time $t_\varphi = 59$ min, then solidification starts. Furthermore, noticeable is that, despite that solidification process is started, L_f continues to increase slightly at the very beginning of the discharge stage, and then decreases monotonically towards 0 at $t_\varphi = 240$ min. The heat stored in the melted PCM continues to melt the remaining solid PCM until the convection becomes negligible. It is worth noticing that this behavior is not observed in the complete melting case because of the imposed temperature at the right wall.

Let us now pay attention to the transfers occurring at the left wall, suddenly submitted to a lower temperature. This is done through the temporal evolution of the Nusselt number, and the temporal-integrated

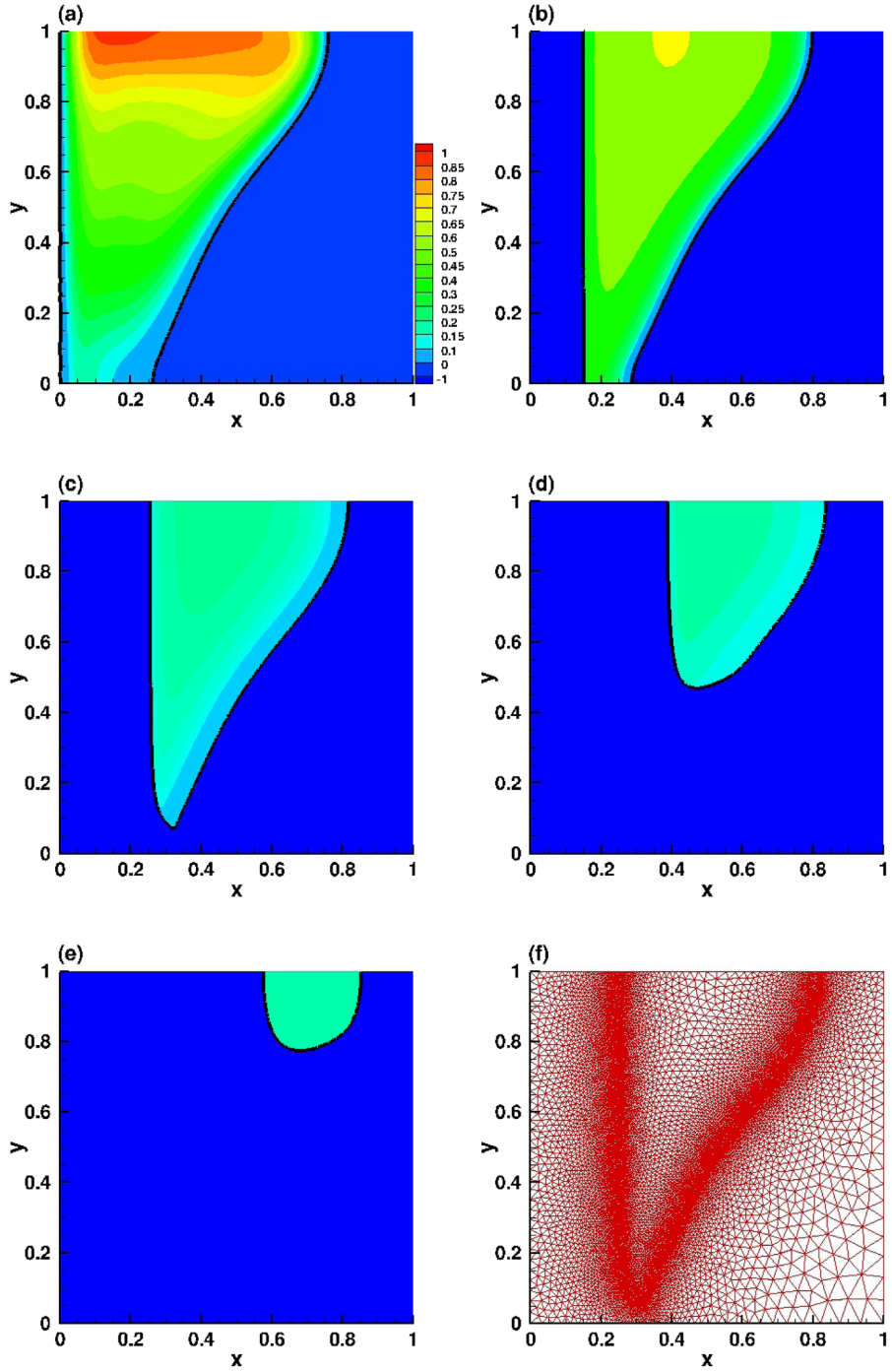

Fig. 11. Solidification of the PCM after a partial melting. Temperature isolines in the liquid phase. The solid part is represented in blue and corresponds to the region of temperature $\theta_{co} \leq \theta_f = 0$. Time instants (panels a to e): $t_\varphi = 59$ min, $t_\varphi = 70$ min, $t_\varphi = 90$ min, $t_\varphi = 131$ min and $t_\varphi = 200$ min. The adapted mesh corresponding to $t_\varphi = 90$ min is plotted in panel (f). $Ra_{co} = 3.27{\cdot}10^5$. (For interpretation of the references to colour in this figure legend, the reader is referred to the web version of this article.)

values of the Nusselt number, or the accumulated heat input.

Panels (c) and (d) of the Fig. 12 illustrate the Nusselt number for the cases CM and PM. The three investigated Rayleigh numbers are shown, with clear differences between them. This difference corroborates with that already reported for the melting case, over shorter times scales. This indicates that the heat transfer during the solidification process is fundamentally different from the melting one.

For the CM case, for $Ra_{co} = 3.27{\cdot}10^5$, the Nusselt number first decreases sharply, for $t_\varphi \leq 18$ min, then it reaches a plateau at $Nu = 7$ during the complete melting. At $t_\varphi = 185$ min, solidification starts and Nu suddenly decreases over very short times, reaching negative values ($Nu \approx -15$). It follows an increase of Nu with time, up to reaching an asymptotic value close to 0 (zero temperature gradients, i.e. uniform temperature at the left wall). The same mechanism is observed over a shorter time interval when Ra_{co} is increased.

For the PM case, the Nusselt number also decreases sharply to a negative value when the solidification starts. However, the convection flow remaining in the melted region influences the heat transfer at the very beginning of the solidification process. The hot fluid in the middle of the melted PCM is advected by the natural convection flow to the

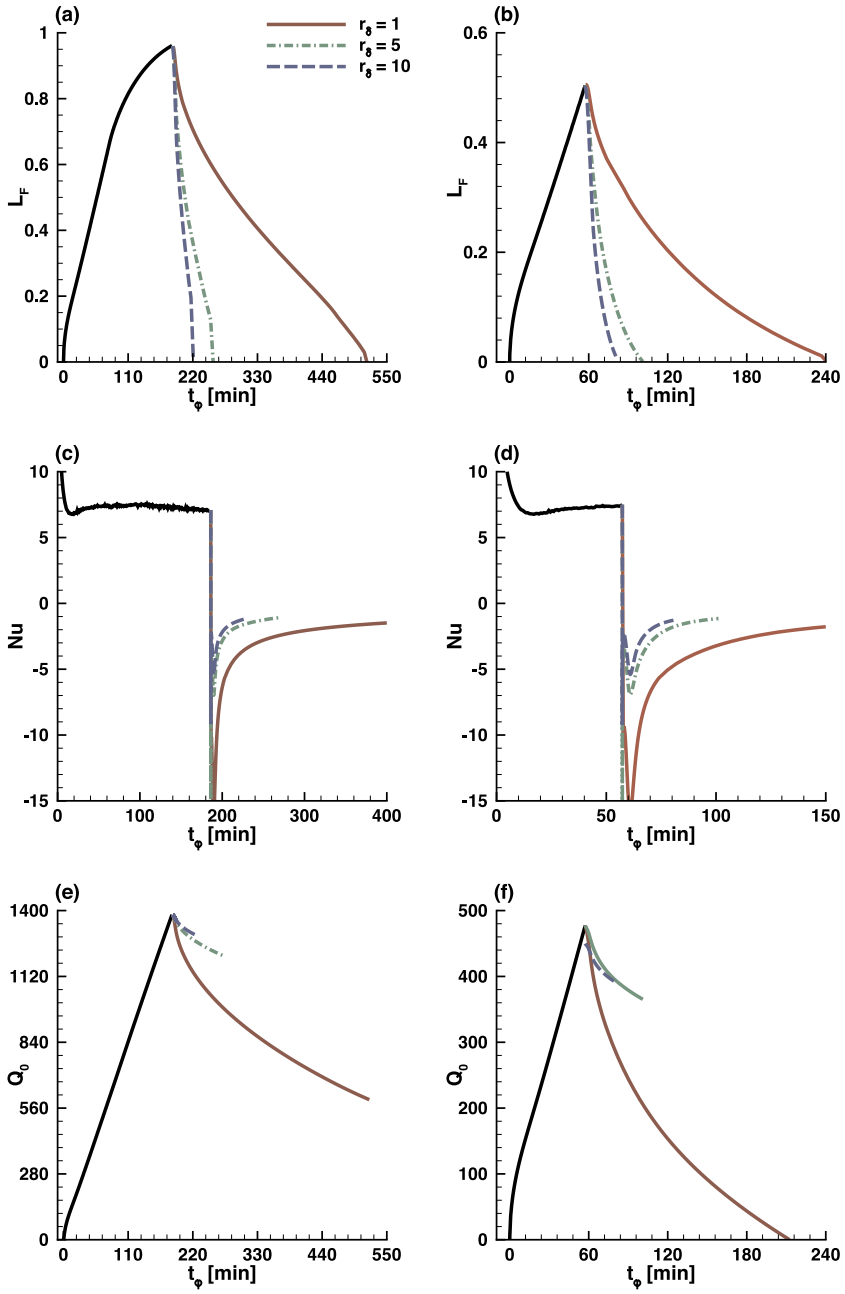

Fig. 12. Temporal evolution of the liquid fraction (L_f), the Nusselt number Nu, and the accumulated heat input Q_0 during the entire melting-solidification cycle. Case CM (left) and case PM (right).

boundaries and induces a temperature gradient at the left wall, resulting into an oscilating behavior of the Nusselt number before reaching asymptotic value. This is in agreement with the previous comment about the melting continuing in the right part of the cavity, despite the solidification has started, and the slight increase of the liquid fraction at the very first time steps of the discharging process.

Both charge and discharge cycles are better illustrated in the time evolution of the accumulated heat Q_0 defined in (25), as it is shown in panels (d) and (e) of Fig. 12. Heat is first stored during the melting stage, corresponding to $t_\varphi \leq 185$ min for CM (Fig. 12(d)) and $\tau \leq 59$ min for PM (Fig. 12(e)), and is then restored during the solidification stage.

The CM case indicates higher value of Q_0 ($Q_0 = 1400$, for $Ra_{co} = 3.27{\cdot}10^5$) compared to the PM case ($Q_0 = 500$), meaning that PCM is more efficient in terms of heat storage. However, PM case exhibits well balanced characteristic times between the solidification and the melting stages for $Ra_{co} = 3.27{\cdot}10^5$. Besides, when the Ra number increases, the stored heat is discharged faster.

Moreover, the temperature and the velocity profiles drop sharply during the first step of the cooling process and become almost equal to zero very early in the whole domain. This means that conduction dominates the solidification process, and the convection becomes rapidly negligible. As a consequence, the melting fronts are vertical and have a symmetric position with respect to the center of the cavity.

5. Final discussion and conclusions

The n-octadecane PCM we simulated in this paper is generally used for buildings purposes, due to its phase change temperature of 28^oC. Zhu et al. (2009) and Kalnæs and Jelle (2015) listed various applications, starting from free cooling, peak load shifting, passive building systems and solar energy storage. For each case, the PCM is assumed to

melt during day-time and to solidify during the night-time.

We have developed and validated a numerical tool based on adaptive finite elements methods to simulate melting and solidification processes of the PCM. Once our tool was validated against available results, we used it to obtain new physical behaviours of PCM and therefore to predict their practical use.

It was noticed that, when the same Rayleigh number is used to compare the melting and solidification cycles, meaning that the charge and the discharge modes occur at the same δT, the solidification is always slower than the melting. This behavior is linked to the heat transfer mode leading each of the cycles. Convective heat transfer dominates indeed the melting process, enhancing thus the heat transfer, while conduction is the main heat transfer mode during the solidification, resulting to a slower operating process. However, when the discharge temperature is decreased by a factor of 5, i.e both Ra_{co} and $r_\delta \times Ste$ are increased by a factor of 5, the solidification and the melting occur over similar times.

A first issue that has been brought up by Ascione et al. (2014) is the difficulty of the PCM systems to completely discharge during night-time. Though, if the PCM does not solidify entirely, the effectiveness of the system may be considerably reduced. In this case, to have a shorter cooling period it is not advised to melt the PCM completely.

However, for solar energy storage applications, full melting of the PCM is needed to utilize its latent heat storage capacity. Hence, a partial melting is not optimal. For other applications, when shorter discharge time is needed, the use of external cooling techniques is needed to ensure a colder discharge temperature.

Acknowledgments

This project was co-financed by the European Union with the European regional development fund (ERDF, HN0002081) and by the Normandy Regional Council via the M2NUM project. The authors are grateful to CRIANN (Centre Régional Informatique et d'Applications Numériques de Normandie, France) for providing computational resources (project 2017005). The authors thank the Reviewers for relevant comments and suggestions.

References

Agyenim, F., Hewitt, N., Eames, P., Smyth, M., 2010. A review of materials, heat transfer and phase change problem formulation for latent heat thermal energy storage systems (lhtess). Renew. Sustain. Energy Rev. 14 (2), 615–628.
Ascione, F., Bianco, N., Masi, R.F.D., de Rossi, F., Vanoli, G.P., 2014. Energy refurbishment of existing buildings through the use of phase change materials: energy savings and indoor comfort in the cooling season. Appl. Energy 113, 990–1007.
Belhamadia, Y., Fortin, A., Chamberland, E., 2004. Anisotropic mesh adaptation for the solution of the Stefan problem. J. Comput. Phys. 194 (1), 233–255.
Belhamadia, Y., Fortin, A., Chamberland, E., 2004. Three-dimensional anisotropic mesh adaptation for phase change problems. J. Comput. Phys. 201 (2), 753–770.
Belhamadia, Y., Kane, A.S., Fortin, A., 2012. An enhanced mathematical model for phase change problems with natural convection. Int. J. Numer. Anal. Model. 3 (2), 192–206.
Bertrand, O., Binet, B., Combeau, H., Couturier, S., Delannoy, Y., Gobin, D., Lacroix, M., Quéré, P.L., Médale, M., Mencinger, J., et al., 1999. Melting driven by natural convection a comparison exercise: first results. Int. J. Therm. Sci. 38 (1), 5–26.
Cao, Y., Faghri, A., 1990. A numerical analysis of phase change problem including natural convection. ASME J. Heat Trans. 112, 812–815.
Cao, Y., Faghri, A., Chang, W.S., 1989. A numerical analysis of Stefan problems for generalized multi-dimensional phase-change structures using the enthalpy transforming model. Int. J. Heat Mass Trans. 32 (7), 1289–1298.
Castro-Diaz, M., Hecht, F., Mohammadi, B., 2000. Anisotropic grid adaptation for inviscid and viscous flows simulations. Int. J. Numer. Methods Fluids 25, 475–491.
Chabot, C., Gosselin, L., 2017. Solid-liquid phase change around a tube with periodic heating and cooling: scale analysis, numerical simulations and correlations. Int. J. Therm. Sci. 112, 345–357.
Danaila, I., Hecht, F., 2010. A finite element method with mesh adaptivity for computing vortex states in fast-rotating Bose–Einstein condensates. J. Comput. Phys. 229, 6946–6960.
Danaila, I., Moglan, R., Hecht, F., Masson, S.L., 2014. A Newton method with adaptive finite elements for solving phase-change problems with natural convection. J. Comput. Phys. 274, 826–840.
Evans, K.J., Knoll, D., Pernice, M., 2006. Development of a 2-D algorithm to simulate convection and phase transition efficiently. J. Comput. Phys. 219 (1), 404–417.
Faghri, A., Zhang, Y., 2006. Transport Phenomena in Multiphase Systems. Elsevier.
Frey, P.J., George, P.L., 1999. Maillages. Hermès, Paris.
George, P.L., Borouchaki, H., 1998. Delaunay Triangulation and Meshing. Hermès, Paris.
Gobin, D., Le Quéré, P., 2000. Melting from an isothermal vertical wall. synthesis of numerical comparison exercise. Comput. Assisted Mech. Eng. Sci. 7 (3), 289–306.
Gong, W., Johannes, K., Kuznik, F., 2015. Numerical simulation of melting with natural convection based on lattice Boltzmann method and performed with Cuda enabled GPU. Commun. Comput. Phys. 17 (5), 1201–1224.
Grigull, U., Sandner, H., 1984. Heat Conduction. Hemisphere Publishing, New York, NY.
Hecht, F., 2012. New developments in FreeFem++. J. Numer. Math. 20, 251–266.
Hecht, F., Mohammadi, B., 1997. Mesh adaptation by metric control for multi-scale phenomena and turbulence. AIAA Pap. 97, 0859.
Hecht, F., Pironneau, O., Hyaric, A.L., Ohtsuke, K., 2007. FreeFem++ (manual). http://www.freefem.org.
Ho, C.J., Chu, C.H., 1993. Periodic melting within a square enclosure with an oscillatory surface temperature. Int. J. Heat Mass Trans. 36 (3), 725–733.
Hosseini, M.J., Rahimi, M., Bahrampoury, R., 2014. Experimental and computational evolution of a shell and tube heat exchanger as a Pcm thermal storage system. Int. Commun. Heat Mass Trans. 50, 128–136.
Jany, P., Bejan, A., 1988. Scaling theory of melting with natural convection in an enclosure. Int. J. Heat Mass Trans. 31 (6), 1221–1235.
Kalnæs, S., Jelle, B., 2015. Phase change materials and products for building applications: a state-of-the-art review and future research opportunities. Energy Build 94, 150–176.
Kheirabadi, A.C., Groulx, D., 2015. The Effect of the Mushy-zone Constant on Simulated Phase Change Heat Transfer. Proceedings of the CHT-15, ICHMT International Symposium on Advances in Computational Heat Transfer, Ichmt Digital Library Online. Begel House Inc., pp. 528–549.
Kowalewski, A., Gobin, D., 2004. Phase Change With Convection: Modelling and Validation. Springer.
Kumar, M., Krishna, D.J., 2017. Influence of mushy zone constant on thermohydraulics of a Pcm. Energy Proc. 109, 314–321.
Ma, Z., Zhang, Y., 2006. Solid velocity correction schemes for a temperature transforming model for convection phase change. Int. J. Numer. Methods Heat Fluid Flow 16 (11), 204–225.
Mencinger, J., 2004. Numerical simulation of melting in two-dimensional cavity using adaptive grid. J. Comput. Phys. 198 (1), 243–264.
Morgan, K., 1981. A numerical analysis of freezing and melting with convection. Comput. Methods Appl. Mech. Eng. 28 (3), 275–284.
Okada, M., 1984. Analysis of heat transfer during melting from a vertical wall. Int. J. Heat. Mass Trans. 27, 2057–2066.
Rubinstein, L., 1947. On the solution of stefan's problem. Bull. Acad. Sci. URSS. Sér. Géograph. Géophys. (Izvestia Akad. Nauk SSSR) 11, 37–54.
Stefan, J., 1891. Über die theorie der eisbildung, insbesondere über die eisbildung im polarmeere. Ann. Phys. 278 (2), 269–286.
Vergez, G., Danaila, I., Auliac, S., Hecht, F., 2016. A finite-element toolbox for the stationary Gross-Pitaevskii equation with rotation. Comput. Phys. Comm. 209, 144–162.
Vidalain, G., Gosselin, L., Lacroix, M., 2009. An enhanced thermal conduction model for the prediction of convection dominated solid-liquid phase change. Int. J. Heat Mass Trans. 52, 1753–1760.
Voller, V.R., Cross, M., Markatos, N.C., 1987. An enthalpy method for convection/diffusion phase change. Int. J. Numer. Meth. Eng. 24, 271–284.
Voller, V.R., Felix, P., Swaminathan, C.R., 1996. Cyclic phase change with fluid flow. Int. J. Number. Methods Heat Fluid Flow 6, 57–64.
Voller, V.R., Prakash, C., 1987. A fixed grid numerical modelling methodology for convection-diffusion mushy region phase-change problems. Int. J. Heat Mass Trans. 30 (8), 1709–1719.
Wang, S., Faghri, A., Bergman, T.L., 2010. A comprehensive numerical model for melting with natural convection. Int. J. Heat Mass Trans. 53, 1986–2000.
Wang, S., Faghri, A., Bergman, T.L., 2010. Numerical modeling of alternate melting and solidification. Numer. Heat Trans. Part B Fund. 58 (6), 393–418.
Yao, L.S., Prusa, J., 1989. Melting and freezing. Advances in Heat Transfer. Vol. 19. Elsevier, pp. 1–95.
Zhang, T., Tang, Q., Lu, H., Wang, S., Sun, L., 2015. Numerical study of melted Pcm inside a horizontal annulus with threads in a three-dimensional model. RSC Adv. 5 (16), 12178–12185.
Zhang, Y., Danaila, I., 2013. Existence and numerical modelling of vortex rings with elliptic boundaries. Appl. Math. Model. 37, 4809–4824.
Zhu, N., Ma, Z., Wang, S., 2009. Dynamic characteristics and energy performance of buildings using phase change materials: a review. Energy Convers. Manage. 50 (12), 3169–3181.